2024 American Control Conference (ACC)
July 8-12, 2024. Toronto, Canada

# Safety Factor Profile Regulation via Self-triggered Model Predictive Control in the EAST Tokamak*

Zibo Wang, Sai Tej Paruchuri, Lixing Yang, Eugenio Schuster

*Abstract*— **The tokamak, a viable option for harnessing nuclear fusion energy, employs strong helical magnetic fields to confine a plasma (ionized gas) within a toroidal vacuum chamber. Optimal performance in tokamaks necessitates sophisticated control mechanisms to shape the spatial profiles of specific plasma properties. One such property is the safety factor $q$, which measures the pitch of the helical magnetic field lines. The dynamics of the $q$ profile in tokamaks depends on the gradient of the poloidal magnetic flux, which is governed by a nonlinear partial differential equation referred to as the magnetic diffusion equation. In this work, model predictive control (MPC) is proposed to regulate the $q$ profile in the EAST tokamak. The finite-horizon optimal control problem (FHOCP) associated with the MPC approach is defined with the goal of minimizing the tracking error between observed and target gradients of the poloidal magnetic flux while satisfying input and state constraints. To address the optimization problem in real time, a simplified model is derived from the magnetic diffusion equation. As a difference from previous efforts in this area, a self-triggered mechanism is implemented within the MPC algorithm to prevent redundant computations arising in fixed sampling-time MPC schemes. Simulation studies show that the proposed controller has the capability of regulating the $q$ profile through the manipulation of the plasma current and the heating and current-drive powers. A comparison with regular fixed-sampling-time MPC methods demonstrates that the proposed self-triggered MPC strategy optimizes performance by avoiding redundant computations and saving computational time.**

## I. Introduction

Nuclear fusion has garnered significant attention as a potentially transformative energy source due to its advantages, such as high energy density, abundant fuel availability, and negligible contributions to air pollution or climate change. Furthermore, the radioactive byproducts of fusion reactions are relatively short-lived compared to fission, minimizing long-term waste management concerns. To increase the likelihood of fusion, the fuel gas (a mix of isotopes of hydrogen) must be heated to extreme temperatures of the order of 100 million degrees. At these temperatures, the fuel gas is found in an ionized plasma state, known as the fourth state of matter. Containing this ionized gas at such high temperatures demands specialized confinement mechanisms. Charged particles within the plasma can be effectively confined through the application of magnetic fields, capitalizing on the Lorentz force to counterbalance the plasma's inherent expansion tendencies. The tokamak, a toroidally-shaped device, has emerged as a particular effective approach to magnetic confinement of the plasma. However, achieving commercial viability for fusion energy may require the operation of tokamaks under a unique set of conditions referred to as Advanced Tokamak (AT) scenarios. These scenarios are characterized by superior confinement properties, enhanced magnetohydrodynamic (MHD) stability, and possible steady-state operation. The effective realization of AT scenarios is intrinsically linked to the ability of meticulously controlling the spatial distribution of several key plasma properties, commonly referred to as "profiles." One such profile is the safety factor $q$, a metric that measures the spatial variation of the pitch of the helical magnetic field lines that are responsible for plasma confinement.

The application of non-inductive heating and current drive techniques is central to achieving optimized plasma profiles and, by extension, AT scenarios. These methods, such as neutral beam injection (NBI) and lower hybrid waves (LHW), serve as actuating mechanisms, facilitating the active control of plasma profiles. Several recent studies have delved into the synthesis of Model Predictive Control (MPC) algorithms for the purpose of $q$ profile regulation [1], [2], [3], [4]. In recent work [4], an offset-free MPC algorithm to regulate the $q$ profile using non-inductive heating and current drives was developed and integrated into the EAST Plasma Control System (PCS) [5] under the Profile Control Category (PCC). However, experimental results highlight the substantial computational costs associated with this MPC implementation, limiting the length of the prediction horizon. Excessive computational requirements by the MPC algorithm would restrict its applicability in scenarios demanding concurrent control of multiple plasma properties using different controllers. Therefore, improved strategies for computational resource allocation are needed, both within the PCC and across the broader PCS landscape.

To overcome these challenges associated with regular MPC techniques, self-triggered MPC solutions have been proposed to reduce unnecessary computations. A self-triggered controller [6] determines the next update time based on the controller performance, which eliminates the need for continuous monitoring and updating arising in regular MPC approaches. The general framework of self-triggered control systems and a comparison between event-triggered and self-triggered control systems is provided in [7]. The stability properties and control performance when the controller operates at variable intervals are studied in [8]. The feasibility of the feedback controller combined with the triggering mechanism has been studied for the self-triggered control of discrete-time linear systems in [9], [10]. Research then

*This work was supported by the U.S. Department of Energy under contract DE-SC0010537.

Z. Wang (zibo.wang@lehigh.edu), S. T. Paruchuri, L. Yang, and E. Schuster are with the Department of Mechanical Engineering and Mechanics, Lehigh University, Bethlehem, PA 18015, USA.

evolved to include more complex situations involving various types of constraints and disturbances [11], [12]. Existing literature on self-triggered MPC confirms its effectiveness in avoiding extra calculations, making it a strong candidate for improving the computational efficiency of the $q$-profile controller in the EAST tokamak. This work focuses on developing and implementing a self-triggered model predictive algorithm for $q$-profile control in the EAST tokamak. The self-triggering condition is based on the mechanism presented and theoretically analyzed in [13]. Extensive numerical simulation results illustrate the quantitative reduction in computational burden when the regular MPC is replaced by the proposed self-triggered MPC.

This paper is organized as follows. Section II introduces the control-oriented models for the $q$ profile and other related plasma properties. Section III summarizes how the control-oriented model is reduced to a form suitable for synthesizing a computationally efficient control algorithm. Section IV formulates the control problem and presents the self-triggered MPC algorithm. Section V presents simulation results comparing self-triggered and regular MPC methods. Conclusions and future work are discussed in Section VI.

## II. Safety Factor Profile Evolution Model

### A. Poloidal Magnetic Flux Dynamics

Details on the tokamak magnetic configuration, variable definitions, and response models can be found in [4], [14]. The $q$ profile is defined as

$$q(\hat{\rho},t) = -B_{\phi,0}\rho_b^2\hat{\rho}\left(\partial\psi/\partial\hat{\rho}\right)^{-1}, \tag{1}$$

where $\hat{\rho}$ is the mean effective minor radius, $t$ is the time, $B_{\phi,0}$ is the vacuum toroidal magnetic field at the major radius $R_0$, $\psi$ is the poloidal stream function defined as $\psi \triangleq \Psi/2\pi$, and $\Psi$ is the poloidal magnetic flux. The $q$ profile can be regulated by controlling the gradient of the stream function. The magnetic diffusion equation (MDE) governs the evolution of the stream function and takes the form

$$\frac{\partial\psi}{\partial t}=\frac{\eta(T_e)}{\mu_0\rho_b^2\hat{F}^2}\frac{1}{\hat{\rho}}\frac{\partial}{\partial\hat{\rho}}\left(\hat{\rho}D_\psi\frac{\partial\psi}{\partial\hat{\rho}}\right)+R_0\hat{H}\eta(T_e)\frac{\langle\bar{j}_{NI}\cdot\bar{B}\rangle}{B_{\phi,0}}, \tag{2}$$

subject to boundary conditions $\frac{\partial\psi}{\partial\hat{\rho}}|_{\hat{\rho}=0}=0$ and $\frac{\partial\psi}{\partial\hat{\rho}}|_{\hat{\rho}=1}=k_{I_p}I_p$, where $I_p$ is the plasma current, $\mu_0$ is the permeability in vacuum, $\eta$ is the plasma resistivity, $T_e$ is the electron temperature, $\hat{F}$, $\hat{G}$ and $\hat{H}$ are geometric factors [15] capturing the topology of the MHD equilibrium, and $\frac{\langle\bar{j}_{NI}\cdot\bar{B}\rangle}{B_{\phi,0}}$ is the non-inductive current drive. The notation $\langle\cdot\rangle$ is used to denote the flux-surface average of a quantity. The terms $D_\psi$ in and $k_{I_p}$ are defined as $D_\psi(\hat{\rho}) \triangleq \hat{F}\hat{H}\hat{G}$ and $k_{I_p} \triangleq -\frac{\mu_0}{2\pi}\frac{R_0}{\hat{G}(1)\hat{H}(1)}$.

### B. Electron Heat Transport Equation

As evident from (2), the evolution of $\psi$ depends on the evolution of the electron temperature $T_e$. When heat diffusion is the dominant transport mechanism, the evolution of $T_e$ can be modeled using a simplified version of the electron heat transfer equation (EHTE), which can be expressed as

$$\frac{3}{2}\frac{\partial}{\partial t}[n_eT_e]=\frac{1}{\rho_b^2\hat{H}}\frac{1}{\hat{\rho}}\frac{\partial}{\partial\hat{\rho}}\left[\hat{\rho}\frac{\hat{G}\hat{H}^2}{\hat{F}}\left(\chi_e n_e\frac{\partial T_e}{\partial\hat{\rho}}\right)\right]+Q_e, \tag{3}$$

with boundary conditions $\frac{\partial T_e}{\partial\hat{\rho}}|_{\hat{\rho}=0}=0$ and $T_e(1,t)=T_{e,bdry}(t)$, where $\chi_e(\hat{\rho},t)$ denotes the electron thermal conductivity and $T_{e,bdry}$ is the temperature at the plasma edge. The total electron heating power density is denoted as $Q_e(\hat{\rho},t)$, which is expressed as $Q_e(\hat{\rho},t)=Q_{ohm}(\hat{\rho},t)+Q_{aux}(\hat{\rho},t)-Q_{rad}(\hat{\rho},t)$, where $Q_{ohm}$ is the ohmic power density, $Q_{rad}$ is the radiation power density, and $Q_{aux}$ is the auxiliary power density. The auxiliary power density is computed by $Q_{aux} \triangleq Q_{NBI}+Q_{LHW}=\sum_{i=1}^{n_{nbi}}Q_{NBI_i}+\sum_{i=1}^{n_{lhw}}Q_{LHW_i}$, where $Q_{NBI}$ and $Q_{LHW}$ are natural beam injection and lower hybrid wave heating profiles, respectively. The evolution of the electron density $n_e$ is modeled as $n_e(\hat{\rho},t)=n_e^{prof}(\hat{\rho})\bar{n}_e(t)$, where $n_e^{prof}$ is a reference electron density profile and $\bar{n}_e$ is the line average electron density.

### C. Plasma Stored Energy Dynamics

Another plasma property that is critical for the MHD stability of the plasma and is coupled to the evolution of the safety factor is the plasma stored energy $W$. A nonlinear first-order differential equation is used to model the dynamics of the volume-averaged plasma stored energy density, i.e.

$$\frac{dW}{dt}=-\frac{W}{\tau_E(t)}+P_{tot}(t)\triangleq f_W, \tag{4}$$

where $\tau_E \propto I_p(t)^{0.96}P_{tot}(t)^{-0.73}\bar{n}_e(t)^{0.4}$ denotes the energy confinement time, which is computed using the $IPB98(y,2)$ scaling law [16]. The total injected power $P_{tot}(t)$ is given by

$$P_{tot}=P_{ohm}+P_{aux}-P_{rad}, \tag{5}$$

where $P_{ohm}$ is the ohmic power, $P_{rad}$ is the radiated power, and $P_{aux}=\sum P_p$ is the total auxiliary-heating and current-drive power ($p\in\{NBI_i, LHW_l\}$, $i\in\{1,\cdots,n_{nbi}\}$, $l\in\{1,\cdots,n_{lhw}\}$).

## III. Control-Oriented Model for MPC

The presented model is reduced in this section to a form that is suitable for MPC implementation. To simplify the coupling between $\psi$ (MDE) and $T_e$ (EHTE), and therefore to obtain a simpler model for the $q$ evolution for control design, a control-oriented model for $T_e$ of the form $T_e(\hat{\rho},t)=T_e^{prof}(\hat{\rho})I_p(t)^\alpha P_{tot}(t)^\gamma\bar{n}_e(t)^\kappa$ is introduced. In this model, $T_e^{prof}$ is a reference electron temperature profile and $\alpha$, $\gamma$, $\kappa$ are positive scaling factors [17]. Incorporating the above simplified model for $T_e$ into (2) and taking the partial derivative on both sides results in a partial differential equation that governs the evolution of the poloidal flux gradient $\theta \triangleq \partial\psi/\partial\hat{\rho}$:

$$\frac{\partial\theta}{\partial t}=\left[\frac{dC_{f_1}}{d\hat{\rho}}\theta+\left(C_{f_1}+\frac{dC_{f_2}}{d\hat{\rho}}\right)\frac{\partial\theta}{\partial\hat{\rho}}+C_{f_2}\frac{\partial^2\theta}{\partial\hat{\rho}^2}\right]u_{diff}+ \sum_i\frac{dC_{j_i}}{d\hat{\rho}}u_{j_i}+\frac{dC_{j_{bs}}}{d\hat{\rho}}\frac{1}{\theta}u_{j_{bs}}-C_{j_{bs}}\frac{1}{\theta^2}\frac{\partial\theta}{\partial\hat{\rho}}u_{j_{bs}}\triangleq f_\theta. \tag{6}$$

In (6), $i\in\{nbi_1,\cdots,nbi_{n_{nb}},lhw_1,\cdots,lhw_{n_{lh}}\}$, $C_{f_1}$,$C_{f_2}$,$C_{j_i}$, and $C_{j_{bs}}$ are functions of $\hat{\rho}$. It is clear from (1) that controlling $\theta$ (see definition) is equivalent to controlling the

$q$ profile. The virtual control inputs $u_{diff}$, $u_{j_i}$ and $u_{j_{bs}}$ are defined in terms of the physical actuators $I_p, P_{tot}$, and $\bar{n}_e$ as

$$u_{diff}(t) \triangleq \sqrt{I_p(t)^{-3\gamma} P_{tot}(t)^{-3\varepsilon} \bar{n}_e(t)^{-3\zeta}}, \tag{7a}$$

$$u_{j_i}(t) \triangleq \bar{n}_e(t)^{(\zeta(\delta-1.5)-1)} \left(I_p(t)^{\gamma} P_{tot}(t)^{\varepsilon}\right)^{(\delta-1.5)} P_i(t), \tag{7b}$$

$$u_{j_{bs}}(t) \triangleq I_p(t)^{-0.5\gamma} P_{tot}(t)^{-0.5\varepsilon} \bar{n}_e(t)^{1-0.5\zeta}. \tag{7c}$$

The values of the coefficients $[\gamma, \varepsilon, \zeta]$ are given by $[0.93, 0.31, -0.59]$ [17]. The boundary conditions take the form $\theta(\hat{\rho}=0,t)=0$, $\theta(\hat{\rho}=1,t)=k_{I_p} I_p(t)$. Note that (7) does not depend on $T_e$. However, the evolution between the $q$ profile and $W$ is still coupled. Typically, the $W$ controller prescribes the total power $P_{tot}$ to regulate the total energy. This, in turn imposes an algebraic constraint on the $q$-profile controller via (5). Alternatively, a single controller can be designed to regulate both the $q$ profile and $W$ simultaneously. In this work, the latter approach is used.

Combining the models for $\theta$ and $W$, given in (4) and (6), respectively, and discretizing the augmented model at $N+1$ spatial nodes $\hat{\rho}_0, \cdots, \hat{\rho}_N$ using the finite-difference method results in a nonlinear ordinary differential equation that governs the evolution of $x(t) = [\theta_1, \cdots, \theta_{N-1}, W]^T \in \mathbb{R}^{N\times 1}$, where $\theta_i(t) = \theta(\hat{\rho}_i, t)$, when driven by the physical inputs

$$u \triangleq [I_p, P_{NBI_1}, P_{NBI_2}, P_{NBI_3}, P_{NBI_4}, P_{LHW_1}, P_{LHW_2}]^T. \tag{8}$$

This implies $n_{nbi} = 4$ and $n_{lhw} = 2$. As shown in [4], using a first order Taylor series approximation and a zero-order hold temporal discretization gives a discrete-time linear model

$$\Delta x_{j+1} = A\Delta x_j + B\Delta u_j, \tag{9}$$

where $\Delta x_j = x_j - x^{ref}$, $\Delta u_j = u_j - u^{ref}$, $x^{ref}$ and $u^{ref}$ are the reference state and inputs vectors used for linearization, respectively. Given a $t_j = j \times \Delta t$, note that $x_j = x(t_j)$ and $u_j = u(t_j)$. The state and input matrices, $A$ and $B$, are time-invariant. To eliminate the effect of model uncertainties on the MPC, the offset-free model based on the velocity form is used. It can be written as

$$\Delta\tilde{x}_{j+1} = A\Delta\tilde{x}_j + B\Delta\tilde{u}_j, \tag{10}$$

where $\Delta\tilde{x}_{j+1} = \Delta x_{j+1} - \Delta x_j$ and $\Delta\tilde{u}_{j+1} = \Delta u_{j+1} - \Delta u_j$.

Owing to intrinsic physical constraints, the system's input remains inherently bounded. As a result, the output also manifests bounded behavior. Thus, it is possible to show that the discrepancy in the safety-factor profiles predicted by the original and linearized models is bounded.

## IV. Self-triggered MPC for EAST

The selection of an MPC approach in this work is justified by its inherent ability to handle system constraints, both on state variables and control inputs, making it applicable to both linear and nonlinear systems. The core feature of MPC is its reliance on a system model for predicting future state variables. These predictions are used to optimize a cost function over a defined prediction horizon, all while satisfying system constraints. The control action is recalculated at each sampling time, with only the initial element of the optimal control sequence applied to the system.

### A. Control Input Constraints

Before formulating the MPC problem, it is essential to state the control input constraints. In the subsequent analysis, 4 NBI and 2 LHW drives are assumed to be available for control. The bounds on $u$ and the rate of change of the plasma current $I_p$ at time $t = t_j$ can be written as

$$u_{min} \preceq u_j \preceq u_{max}, \quad \left(\frac{dI_p}{dt}\right)_{min} \leq \left.\frac{dI_p}{dt}\right|_j \leq \left(\frac{dI_p}{dt}\right)_{max}, \tag{11}$$

where $u_{min} \in \mathbb{R}^{7\times 1}$ and $u_{max} \in \mathbb{R}^{7\times 1}$ are lower and upper bounds of $u_j$, respectively, $(dI_p/dt)_{min}$ and $(dI_p/dt)_{max}$ are the minimum and minimum ramp-down/up rates of $I_p$.

### B. Formulation of the MPC Problem

Since the goal is to minimize the tracking error and the feedback control effort over a horizon, the to-be-minimized cost function is defined as

$$J = \sum_{n=j}^{j+N_p-1} \frac{(x_n^J)^T Q_n x_n^J}{2} + (d\Delta u_n)^T R_n d\Delta u_n, \tag{12}$$

where $Q_n$ and $R_n$ are positive-definite weighting matrices, $N_p$ is the horizon length, and $x_n^J = (\Delta\tilde{x}_{n+1} - \Delta\tilde{x}_{n+1}^{tar})$. Define the augmented vector $X_j$ as $X_j \triangleq [(d\Delta u_j)^T, (\Delta\tilde{x}_{j+1})^T]$. By concatenating the augmented vectors $X_j$ from the present time step $t = t_j$ to the penultimate prediction time step $t = t_{j+Np-1}$ in the horizon, we get a vector $\bar{X}$ of the form $\bar{X} \triangleq [X_j^T, X_{j+1}^T, \cdots, X_{j+N_p-1}^T]^T$. Now, the minimization of the cost function (12), subject to the state constraints imposed by the velocity form of the system model (10) and the constraints on physical actuators, can be written as a linearly constrained quadratic programming problem as

$$\min_{\bar{X}} \quad \frac{1}{2}\bar{X}^T P \bar{X} + f \cdot \bar{X} \tag{13}$$

$$\text{subject to} \quad b_{eq} = A_{eq}\bar{X}, \quad b_{in} \succeq A_{in}\bar{X}, \tag{14}$$

where $P$ is a positive-definite diagonal matrix and $f$ is a row vector. Note that the equality constraint in (14) is determined by (10) over the prediction horizon. Also, the inequality constraint in (14) is a variation of (11) over the prediction horizon. In the numerical simulations discussed in the next section, the fast quadratic programming (QP) solver implemented in [4] is used to find solutions for the optimization problem (13)-(14). It is worth noting that the control strategy $u_j^*$ implemented in the plant at time $t_j$ is obtained by extracting $d\Delta u_j{}^*$ from the solution $\bar{X}_j^*$ of the optimization problem discussed above and then using the formula $u_j^* = \Delta u_{j-1} + d\Delta u_j{}^* + u_j^{ref}$.

### C. Self-trigger Condition for MPC

In a regular MPC, the optimization problem presented in the above subsection is solved at every time step $t_j$. To minimize the necessity of solving the optimization problem and balance the trade-off between performance and computational or communication cost, a self-triggered MPC solves the optimization problem at "trigger time steps", which are determined by a specific triggering criteria. Suppose the

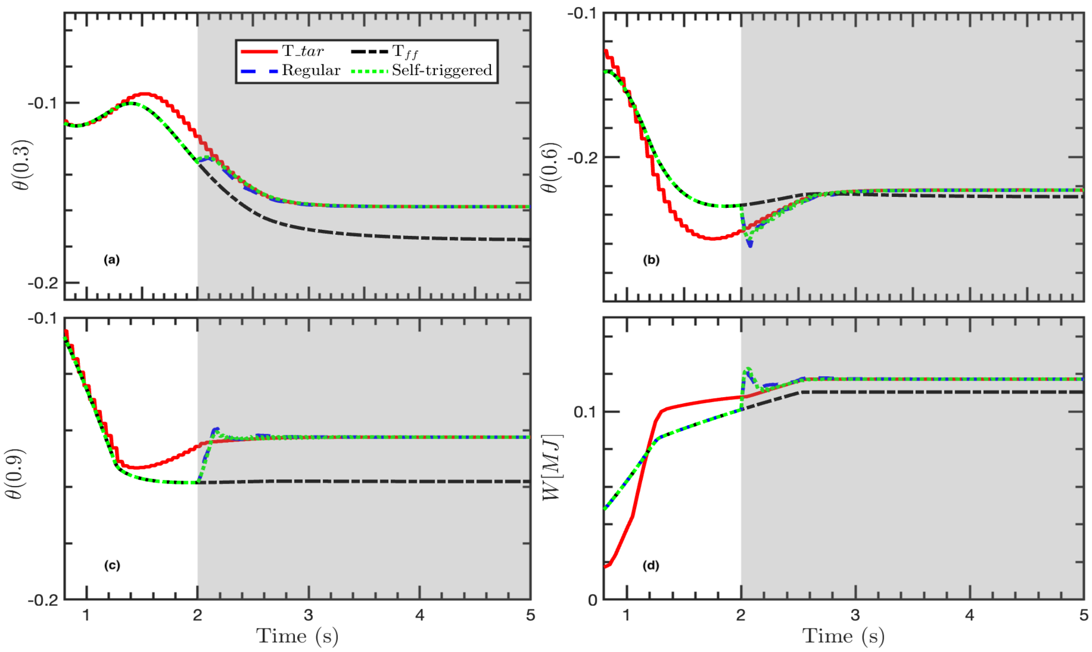


Fig. 1. Comparison of regular and self-triggered MPC tracking results. The first three plots (i.e., (a), (b), and (c)) show the $\theta$ evolution at three different spatial points, and the last plot (d) shows the regulation results for the plasma stored energy.

current trigger time step is $t_k$, then the next trigger time step $t_{k+1}$ is given by $t_{k+1} = t_k + \Gamma_k$, where $\Gamma_k$ is the self-trigger interval defined as

$$\Gamma_k \triangleq \max\left\{T_s - k_e \left\| x_k - \hat{x}_k|_{u^*_{k-1}} \right\|, T_m\right\}. \tag{15}$$

In the above definition, $T_s$ represents the upper bound on the sampling interval, $T_m$ serves as the baseline sampling interval, and $k_e \in \mathbb{R}^+$ is a predefined constant. The term $x_k$ denotes the current measured state. On the other hand, $\hat{x}_k|_{u^*_{k-1}}$ is the state predicted by the linearized model (10) given initial condition $\bar{x}_{k-1}$ and constant input $u^*_{k-1}$. Thus, if there is a substantial deviation between the state predicted by the linearized model and the actual measured state, then the control algorithm is triggered sooner and vice versa. Under certain assumptions, the stability and feasibility of the MPC algorithm equipped with the above defined self-trigger criteria can be proved using the approach shown in [13].

The self-triggered MPC algorithm, outlined in Algorithm 1, operates in a sequential manner to optimize the control inputs while minimizing the computational overhead. Initiated with an initial state $x_0 = x(t_0)$, the algorithm progresses through iterative cycles, each commencing with the sampling of the system state $x_k = x(t_k)$ at time $t = t_k$. Following this, the algorithm calculates the self-trigger interval $\Gamma_k$ using (15). The next sampling time $t_{k+1}$ is determined by adding the dynamically computed interval $\Gamma_k$ to $t_k$. Subsequently, the Fixed Horizon Optimal Control Problem (FHOCP) expressed by (13)-(14) is solved to determine the optimal control input $u^*_k$. This control input is then deployed into the plant for the time span $t \in [t_k, t_{k+1})$. In parallel, the control input is also used to predict $\hat{x}_{k+1}|_{u^*_{k-1}}$, that is necessary for computing $\Gamma_{k+1}$ at the next time step $t_{k+1}$. At $t_{k+1}$, the algorithm repeats the above listed steps.

**Algorithm 1:** Self-Triggered MPC Algorithm

**Require:** Initial state $x(t_0)$
**Initialize** $t_0$, $u^*_0$
**for** $k = 0, 1, 2, \ldots$ **do**
  Sample the state $x(t_k)$ at $t = t_k$
  Compute the self-triggered sampling interval $\Gamma_k$ using (15)
  Solve the FHOCP (13)-(14) to obtain $u^*_k$
  Implement control $\bar{u}^*_k$ into (10) for $t \in [t_k, t_{k+1})$
  Set $t_{k+1} = t_k + \Gamma_k$ and go to next iteration
**end for**

## V. Simulation and Comparison Studies

### A. One-dimensional Simulations Using COTSIM

In this work, the Control-Oriented Transport Simulator (COTSIM) is used as the platform for carrying out the simulation studies. COTSIM, developed based on MATLAB/Simulink, is a one-dimensional transport code designed for simulating tokamak plasma discharges. The code is capable of executing these simulations rapidly, making it suitable for control design applications. The simulator accepts input parameters such as plasma current, desired line-averaged electron density, and auxiliary heating and current drive powers. These inputs are processed through various submodules to calculate essential plasma properties like plasma resistivity, heat deposition, and transport coefficients. The submodules include neural network-based models that act as fast approximations to high-fidelity, physics-based algorithms [18], thus balancing predictive accuracy and computational speed. For thermal conductivity $\chi_e$ in (3), COT-

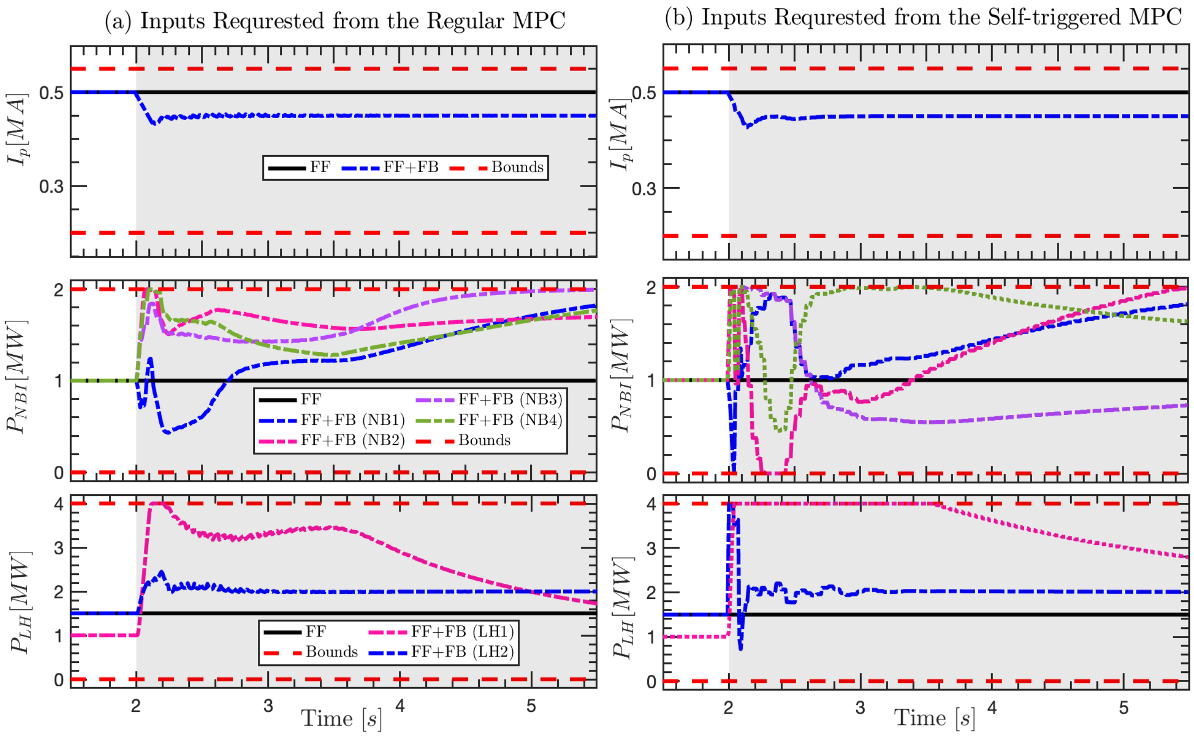


Fig. 2. Comparison of the inputs controlled by the regular (column (a)) and self-triggered (column (b)) MPC schemes. Each set of three plots shows the plasma current, NBI powers, and LHW powers. In addition, each plot compares both FF and FF+FB evolutions with their respective bounds.

SIM allows for the selection of transport and source models from an existing library, which includes both empirical and analytical models such as the Bohm/Gyro-Bohm or Coppi-Tang models.

The COTSIM version used for the simulations relevant to this work includes solvers for the MDE (2) and EHTE (3). The electron thermal conductivity is computed using the Coppi-Tang model. NUBEAMnet [18] is used to model the NBI sources, while simpler models as those presented in Section II are used for the LHW sources. A fixed boundary MHD equilibrium is assumed. The predictive models used for the simulation studies are significantly more complex than those used for control synthesis, which represents a test of robustness for the proposed controllers.

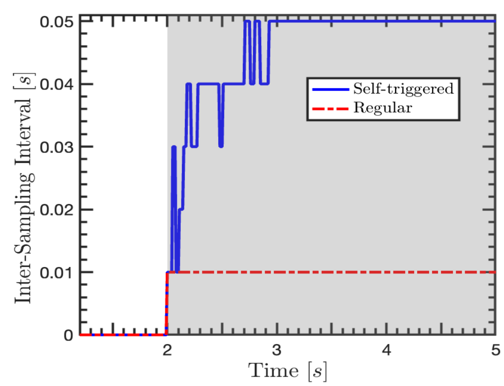


Fig. 3. History of computation periods.

### B. Feedback Simulation Test

To evaluate the performance of the proposed self-triggered MPC scheme, both regular MPC and self-triggered MPC are implemented and tested within the COTSIM environment. Initially, a feedforward simulation is run with a specific input $u_1$ to generate a reference trajectory $\mathrm{T}_{ff}$. A modified input $u_2$ is then used in another feedforward simulation to create a feasible target trajectory $\mathrm{T}_{tar}$ for controller validation. The feedback simulations are then carried out with the feedforward input $u_1$ to assess the ability of the controllers to steer the system towards the feasible target trajectory $\mathrm{T}_{tar}$.

Feedback simulations with varying MPC horizon lengths are carried out to examine the computational demands of regular and self-triggered MPC algorithms. The total plasma discharge, i.e., the simulation duration, is 6 seconds, and the MPC controller is turned on between 2-6 seconds. The constant $k_e$ in (15) is set as 5, the upper bound of the sampling interval $T_s$ is set as 0.05 $s$, and the baseline sampling interval $T_m$ is set as 0.01 $s$.

Fig. 1 compares the regular and self-triggered MPC performance in closed-loop simulations when the predictive horizon is set to 12. As shown in the figure, both regular and self-triggered MPC regulate the $\theta$ profile and $W$ to their corresponding target values by manipulating actuators as shown in Fig. 2. The figures indicate no qualitative difference in terms of control performance between the two MPC algorithms. Thus, self-triggered MPC achieves control regulation similar to that of a regular MPC, however, at a lower computational cost. Fig. 3 shows the self-trigger intervals $\Gamma_k$ when the predictive horizon is 12. In the case of regular MPC, the controller is invoked at each time step. In contrast, the self-triggered MPC initially has a similar trigger interval as the regular MPC. However, over time, its triggering interval gradually extends until it reaches the maximum allowable trigger interval $T_s$. After 3 seconds, the trigger interval stays at 0.05 seconds. This corresponds to the time when the $\theta$ and $W$ values (Fig. 1) converge. Thus, after 3 seconds, the computational burden is significantly reduced when the self-triggered MPC is used. Consequently, the EAST PCS could allocate its resources to regulate other critical plasma properties. Similar patterns of trigger intervals are observed when the prediction horizon is changed.

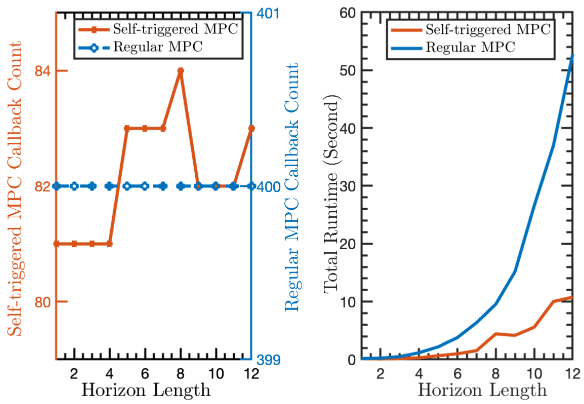


Fig. 4. Callback counts and runtime comparisons between the regular and self-triggered MPC schemes with different prediction horizon lengths.

Fig. 4 (left) shows the number of times the regular and self-triggered MPCs solve the FHOCP for different horizon lengths $N_p$. The blue and red lines denote performances by the regular MPC and the self-triggered MPC, respectively. As shown in the figure, the number of iterations is reduced by more than a factor of 4 when self-triggered MPC is implemented to drive the $q$ profile to its target. Fig. 4 (right) illustrates the cumulative time consumed by the feedback control algorithms. Note that these times correspond to the simulation times in MATLAB and not the actual EAST PCS times. It is found that the cumulative computation time of self-triggered MPC (red line) is less than that of regular MPC (blue line), particularly at longer prediction horizons.

## VI. Conclusions and Future Work

This study proposes a self-triggered MPC scheme for $q$-profile control in the EAST tokamak, and presents an analysis of the comparative performance of regular and self-triggered MPC schemes, utilizing the COTSIM simulation environment. The simulation results, substantiated by multiple test cases with varying prediction horizons, overwhelmingly illustrate the efficacy of the proposed self-triggered MPC in terms of computational efficiency. Moreover, despite the higher computational efficiency, the self-triggered MPC achieves a control performance that is qualitatively similar to the regular MPC. Thus, $q$-profile control using self-triggered MPC could be advantageous to free computational resources that could be used by concurrent controllers regulating other critical plasma properties during experiments. Future work could focus on experimentally testing the proposed self-triggered MPC in the EAST PCS and expanding the control objectives to include other plasma properties.

## References


[1] E. Maljaars, F. Felici, T. Blanken, C. Galperti, O. Sauter, *et al.*, "Profile control simulations and experiments on TCV: a controller test environment and results using a model-based predictive controller," *Nuclear Fusion*, vol. 57, no. 12, p. 126063, 2017.

[2] D. Moreau, S. Wang, E. Witrant, J. Qian, and Q. Yuan, "Model-predictive kinetic control experiments on EAST," in *Proc. 28th IAEA Fusion Energy Conf.*, IAEA, 2021.

[3] S. T. Paruchuri, Z. Wang, T. Rafiq, and E. Schuster, "Model predictive current profile control in tokamaks by exploiting spatially moving electron cyclotron current drives," *Fusion Engineering and Design*, vol. 192, p. 113796, 2023.

[4] Z. Wang, H. Wang, E. Schuster, Z. Luo, Y. Huang, Q. Yuan, B. Xiao, D. Humphreys, and S. T. Paruchuri, "Implementation and initial testing of a model predictive controller for safety factor profile and energy regulation in the EAST tokamak," in *2023 American Control Conference (ACC)*, pp. 3276–3281, IEEE, 2023.

[5] B. Xiao, D. Humphreys, M. Walker, A. Hyatt, J. Leuer, D. Mueller, B. Penaflor, D. Pigrowski, R. Johnson, A. Welander, *et al.*, "EAST plasma control system," *Fusion engineering and design*, vol. 83, no. 2-3, pp. 181–187, 2008.

[6] M. Velasco, J. Fuertes, and P. Marti, "The self triggered task model for real-time control systems," in *Work-in-Progress Session of the 24th IEEE Real-Time Systems Symposium (RTSS03)*, vol. 384, pp. 67–70, Citeseer, 2003.

[7] W. P. Heemels, K. H. Johansson, and P. Tabuada, "An introduction to event-triggered and self-triggered control," in *2012 ieee 51st ieee conference on decision and control (cdc)*, pp. 3270–3285, IEEE, 2012.

[8] A. Anta and P. Tabuada, "To sample or not to sample: Self-triggered control for nonlinear systems," *IEEE Transactions on automatic control*, vol. 55, no. 9, pp. 2030–2042, 2010.

[9] J. B. Berglind, T. Gommans, and W. Heemels, "Self-triggered MPC for constrained linear systems and quadratic costs," *IFAC Proceedings Volumes*, vol. 45, no. 17, pp. 342–348, 2012.

[10] F. D. Brunner, M. Heemels, and F. Allgöwer, "Robust self-triggered mpc for constrained linear systems: A tube-based approach," *Automatica*, vol. 72, pp. 73–83, 2016.

[11] E. Aydiner, F. D. Brunner, W. Heemels, *et al.*, "Robust self-triggered model predictive control for constrained discrete-time lti systems based on homothetic tubes," in *2015 European Control Conference (ECC)*, pp. 1587–1593, IEEE, 2015.

[12] C. Liu, H. Li, J. Gao, and D. Xu, "Robust self-triggered min–max model predictive control for discrete-time nonlinear systems," *Automatica*, vol. 89, pp. 333–339, 2018.

[13] L. Yang, S. Dauchert, and X. Wang, "A framework for predictive control of sampled-data systems using sporadic model approximation," in *2021 American Control Conference (ACC)*, pp. 4686–4691, IEEE, 2021.

[14] Z. Wang, H. Wang, E. Schuster, Z. Luo, Y. Huang, Q. Yuan, B. Xiao, and D. Humphreys, "Optimal shaping of the safety factor profile in the EAST tokamak," in *2021 IEEE Conference on Control Technology and Applications (CCTA)*, pp. 63–68, IEEE, 2021.

[15] Y. Ou, T. Luce, E. Schuster, J. Ferron, M. Walker, C. Xu, and D. Humphreys, "Towards model-based current profile control at DIII-D," *Fusion Engineering and Design*, vol. 82, no. 5-14, pp. 1153–1160, 2007.

[16] ITER EDA *et al.*, "ITER Physics Basis Editors," *Nuclear Fusion*, vol. 39, no. 12, pp. 2201–2215, 1999.

[17] Z. Wang, E. Schuster, T. Rafiq, Y. Huang, Z. Luo, Q. Yuan, B. Xiao, and D. Humphreys, "Refinement of control-oriented model via transp-based transport analysis to enable systematic model-based scenario planning in EAST," *Bulletin of the American Physical Society*, vol. 66, 2021.

[18] Z. Wang, S. Morosohk, T. Rafiq, E. Schuster, M. D. Boyer, and W. Choi, "Neural network model of neutral beam injection in the EAST tokamak to enable fast transport simulations," *Fusion Engineering and Design*, vol. 191, p. 113514, 2023.